Absolutely calibrated, time-resolved measurements of soft x rays using transmission grating spectrometers at the Nike Laser Facility

J. L. Weaver
Plasma Physics Division, Naval Research Laboratory, Washington, D.C. 20375

U. Feldman and J. F. Seely
Space Science Division, Naval Research Laboratory, Washington, D.C. 20375

G. Holland
SFA, Inc., 1401 McCormick Drive, Landover, Maryland 20785

V. Serlin
Plasma Physics Division, Naval Research Laboratory, Washington, D.C. 20375

M. Klapisch
Artep, Inc., Columbia, Maryland 21044

D. Columbant and A. Mostovych
Plasma Physics Division, Naval Research Laboratory, Washington, D.C. 20375

Accurate simulation of pellet implosions for direct drive inertial confinement fusion requires benchmarking the codes with experimental data. The Naval Research Laboratory (NRL) has begun to measure the absolute intensity of radiation from laser irradiated targets to provide critical information for the radiatively preheated pellet designs developed by the Nike laser group. Two main diagnostics for this effort are two spectrometers incorporating three detection systems. While both spectrometers use 2500 lines/mm transmission gratings, one instrument is coupled to a soft x-ray streak camera and the other is coupled to both an absolutely calibrated Si photodiode array and a charge coupled device (CCD) camera. Absolute calibration of spectrometer components has been undertaken at the National Synchrotron Light Source at Brookhaven National Laboratories. Currently, the system has been used to measure the spatially integrated soft x-ray flux as a function of target material, laser power, and laser spot size. A comparison between measured and calculated flux for Au and CH targets shows reasonable agreement to one-dimensional modeling for two laser power densities. © *2001 American Institute of Physics.* [DOI: 10.1063/1.1412862]

I. INTRODUCTION

Production of x-ray emission from laser irradiation has been a vital area of research in laser-plasma physics and for the inertial confinement fusion (ICF) community.[1,2] Soft x-ray radiation is a key to the radiatively preheated pellet design proposed by the Nike laser group as a viable scenario for direct drive ICF.[3] In this design, an early foot of the laser pulse strikes an outer high-Z layer (Au or W) and creates a pulse of soft x-rays that is mainly absorbed by an underlying ablation layer of low density hydrocarbon (CH). The main fuel is minimally heated by this early emission. The preheated foam layer should experience reduced Rayleigh–Taylor instability during compression and the initially low temperature of the main fuel improves the compression efficiency. One-dimensional (1D) simulations of these direct drive implosions (with laser zooming) predict pellet gains of 100 or more.[4] One of the major aims of the present research is to benchmark the radiation part of the radiation hydrodynamics code by measuring the absolute intensity radiated in controlled experiments. To this aim, two transmission grating spectrometers have been installed at the Nike laser to record the absolute intensity of soft x-rays from planar targets as a function of time. This paper describes in detail the experimental setup and the data obtained. In addition, we present a brief comparison of the spectroscopic observations with the spectral distributions predicted by the simulations.

Transmission grating spectrometers have been built for both astrophysical and laboratory observations.[5–14] Advantages of this type of instrument include its simplicity, its flexibility and its reliability as an absolute spectral radiometer. Although the instrument only supplies modest spectral resolution ($\lambda/\delta\lambda \sim 10$–$100$), it can provide broadband ($10\ \text{Å} < \lambda < 150\ \text{Å}$) measurements with time resolution. The transmission grating spectrometer fills an intermediate position between a high spectral resolution ($\lambda/\delta\lambda > 1000$), time-integrating grazing-incidence spectrometer and a low spectral resolution ($\lambda/\delta\lambda < 5$), time resolving set of calibrated filtered diodes already in use at the Nike facility.

The two transmission grating spectrometers installed at Nike laser are distinguished from previous instruments by the incorporation of three independent detection systems. One spectrometer uses a combination of a Si photodiode array and a charge-coupled device (CCD) proximity-coupled to a phosphor scintillator while the adjacent spectrometer uses a streak camera. The multiple systems are nearly along the same line of sight, so they provide complementary data
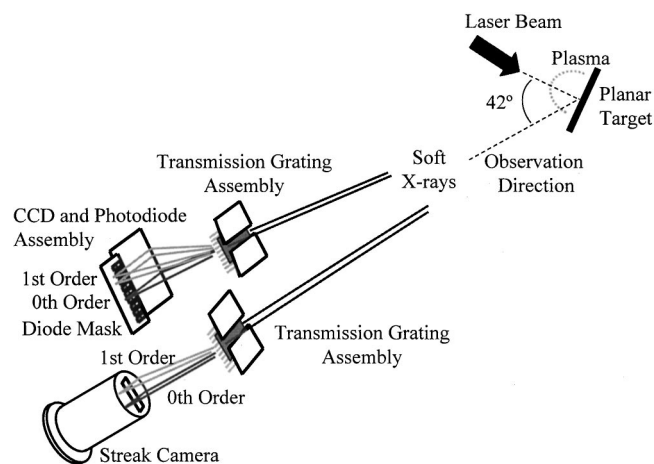
FIG. 1. The spectrometer contains two complete systems with identical transmission grating assemblies. Both systems view the target plasma at approximately 42 degrees relative to the target normal (i.e., the path of the laser beam). One system uses a soft x-ray streak camera for detection while the other uses a combination of a CCD with a phosphor scintillator and an array of Si photodiodes placed in front of the CCD/scintillator. An aperture mask has been placed over the diode that also partially covers the CCD. The image of the apertures can be used to find the position of the diode array relative to the undiffracted light (zero order) of the transmission grating.

for each laser shot. The CCD/phosphor combination provides a time-integrated spectra with the full spectral resolution of the instrument. The Si photodiode array provides modest time resolution ($\sim$0.5 ns) with modest spectral resolution (each diode covers $\sim$4.7 Å) and an absolutely calibrated responsivity. The streak camera provides the same spectral resolution as the CCD/phosphor combination with better time resolution than the Si photodiodes ($\sim$50 ps). Lastly, an aperture mask has been aligned to the Si photodiodes and is designed to extend beyond the photodiodes to partially obscure the CCD. The resulting shadow on the CCD provides an absolute position reference for the photodiodes relative to the time-integrated spectrum. The CCD image can then be used to determine the wavelength coverage of each photodiode after every laser shot. The combined diode array and mask structure can be easily moved along the dispersion direction so the diodes can monitor a variety of wavelengths. In short, these two instruments provide absolutely calibrated, time resolved emission measurements with over accurately defined wavelength regions with modest spectral resolution and redundancy for internal consistency checks.

In Sec. II of this paper, the layout of the transmission grating spectrometer is discussed in detail. Section III presents the step required to derive the absolute intensity of soft x-rays recorded by the spectrometer. Section IV briefly presents the typical data from the spectrometer while Sec. V discusses the comparison between the measurements and the theoretical results.

II. EXPERIMENTAL PROCEDURE

Figure 1 shows the main components of the transmission grating spectrometer. The spectrometer is comprised of two independent but similar instruments. In each, radiation from the target plasma reaches a detector system after passing through an assembly containing an adjustable entrance slit, a transmission filter (free-standing Ti foil), and a gold transmission grating. One detector system is a soft x-ray streak camera and the other is a combination of Si photodiodes and a charge-coupled device (CCD) array coupled to a phosphor scintillator. Although the spectra presented here are spatially integrated, spatially resolved spectra have been recorded by positioning an aperture between the plasma and the spectrometer.

The CCD camera was proximity-coupled to a phosphor scintillator (gadolinium oxysulfide doped with terbium) to convert the incident soft x-rays into visible light. While the camera's 524$\times$760 array of 48 μm$\times$48 μm pixels provided relatively detailed time-integrated spectra, the total sensitivity of the phosphor/CCD combination could not be readily and reliably calibrated to yield an absolute measurement. The Si photodiode array provided less spectral resolution than the CCD, but could provide time-resolved absolute measurements. The Si photodiode array consisted of ten photodiodes each approximately 1.014 mm wide and 1.014 mm tall (0.054 mm separation between elements) was covered by a mask with apertures 0.818 mm wide and 2.8 mm tall (i.e., tall enough to cast a shadow over the CCD, see Sec. I). The target radiation that enters the spectrometer slits is dispersed by the transmission grating and is incident on the CCD and the photodiodes. To avoid edge effects caused by the finite height of the entrance slit, the diodes were aligned to be near the central portion of the image of the entrance slit. A time-integrated spectrum from the target was recorded on the unobscured section of the CCD camera. In addition, the aperture mask leaves a shadow on the CCD image that provided a means of locating the exact wavelength range seen by each element in the Si photodiode array. Each photodiode was connected to a simple circuit that allowed the application of a reverse bias voltage of 90 V and the monitoring of the diode current with a 1 GHz band pass oscilloscope.

The x-ray streak camera system consisted of a streak tube whose output was intensified by a microchannel plate (MCP) intensifier which was lens-coupled to a CCD camera. The streak camera used one of two types of photocathodes. The more sensitive photocathode comprised a 300 Å thick Ti grounding layer, a 1000 Å thick plastic (Lexan) support substrate, and a $\sim$1200 Å thick photoemissive layer (KBr) for photoelectron production. A more robust, although less sensitive, photocathode composed of 1000 Å thick Au was also used. Since the entrance slit of the streak camera was 200 μm wide, a time resolution better than 50 ps was achieved. The streak camera system was aligned such that the transmission grating zero order fell outside the entrance slit of the camera. This alignment prevented distortion of the streak camera image due to large signals due to undiffracted light.

The key optical element in each system within the spectrometer was a 2500 lines/mm gold transmission grating. This type of grating is comprised of an array of fine uniformly spaced, parallel gold bars supported by coarser gold meshes. Advantages in this type of grating include the ease and reliability of its calibration as well as their simple dispersive properties. The plate factor ($\delta\lambda/\delta x$) for the normal incidence arrangement depends linearly on the grating period

(d) and diffraction order (m) and inversely to the grating-detector separation (D), i.e., $\delta\lambda/\delta x \sim md/D$. The expected full width at half maximum (FWHM) for a transmission grating spectrometer can be estimated from a simple formula:

$$\delta\lambda \approx \frac{d(S+W_s)}{R} + \frac{dW_s}{D}, \tag{1}$$

where S is the diameter of the source, R is the distance from the source to the entrance slit, W_s is the width of the entrance slit. Although the grating period (4000 Å/period) and entrance slit width (60 μm) were the same for both spectrometers, the source-grating and grating-detector distances for the streak camera ($R=1500$ mm, $D=700$ mm) and the CCD/photodiode arrays ($R=1206$ mm, $D=688.7$ mm) were slightly different. The instrumental resolution at the CCD array is $\sim$3.03 Å when the nominal laser spot diameter (S) is 750 μm. The spectrometers' resolution in our case is dominated by the first term of Eq. (1)—the spectral resolution is source size limited. Note, for the above arrangement, the plate factor indicates that each masked diode (0.818 mm wide) covers a spectral range of $\sim$4.7 Å, slightly larger than the expected instrumental width.

The transmission grating spectrometers were installed on a port that was at an angle of 42° from the target normal. The dispersion direction for both spectrometers was primarily in a vertical orientation. One to ten beams of the Nike laser were used for the shots with a typical energy of 20–40 J/beam, a pulse duration of 4 ns, and a focal spot size (FWHM) of ranging from 750 μm to 1500 μm. The prepulse (foot) intensity was typically less than 2% that of the main pulse. The power density on target ranged from 3×10^{11} to 2×10^{13} W cm^{-2}. Planar targets of CH and Au of varying thickness (from 12.5 to 100 μm) were irradiated.

III. SYSTEM CHARACTERIZATION

The data analysis for the spectrometer described in Sec. I must take into account the various components of the system. The dispersed radiation that reaches the Si photodiodes represents the total number of photons incident on the entrance slit of the spectrometer, transmitted through the Ti filter, diffracted by the grating onto the collection area of the diode, and converted into current within the diode. A radiometric expression for this measurement begins with the basic equation:[15]

$$V = \int\int\int L(x,y,z,\theta,\varphi,\lambda,t)G(x,y,z,\theta,\varphi,\lambda,t)$$
$$\times d\Omega_{\text{source}}\, dA_{\text{slit}}\, d\lambda, \tag{2}$$

where V is the voltage measured at the diode, L is the radiance of the target (W cm^{-2} Å^{-1} ster^{-1}), G is the response function for the spectrometer, and the variables of integration have their normal definitions as solid angle of source at the slit, collection area of the slit, and wavelength coverage of the detector element. The radiance and the response functions can depend on spatial coordinates (x,y,z), observation angles (θ,φ), wavelength (λ), and time (t). Since the spectrometer lacks spatial resolution, the radiation collected at

the entrance slit represents an integral of the radiance over the emission region from the spectrometer's narrow field of view about a 42° line of sight from the target normal. The measurement determines the average value of the radiance, $\bar{L}$, for the field of view and the area of the slit. The spatial and angular dependencies will be further discussed in Sec. V as part of the comparison between the experimental and theoretical results for the emission.

The large distance of the spectrometer from the target ($\sim$1203 mm) and the small size of the target plasma ($\sim$1 mm) and photodiode ($\sim$1 mm) allow the above integrals to be approximated. The solid angle of the source at the spectrometer, $d\Omega_{\text{source}}$ can be taken as the projected area of the source divided by the square of the source-slit separation distance, $\Delta\Omega_{\text{source}}\approx(\cos(\theta_{\text{view}}\approx42°)\Delta A_{\text{source}})/R^2$. The source area is assumed to be determined by the diameter of the laser focal spot, S, $[\Delta A_{\text{source}}\sim\pi(S/2)^2]$. Previous imaging of the soft x-ray emission using a multilayer telescope indicated that the size of the emission region is comparable to the laser focal spot.[16] The collection area of the slit (dA_{slit}) is taken to be the product of the slit width (W_s) and the effective height of the slit (H_{slit}). Since the actual slit height (7.6 mm) is much greater than that of the diode ($H_{\text{diode}}=1.014$ mm), the effective height of the entrance slit is determined by the height of the diode translated to the location of the slit, i.e., $H_{\text{slit}}\sim H_{\text{diode}}[R/(R+D)]$ where R is again the target-slit separation distance and D is the slit-diode distance. The response function for the spectrometer is given by the product of the transmission factor for the filter (T_{filter}), the diffraction efficiency of the grating ($\epsilon_{\text{grating}}$), the diode responsivity (ρ_{diode}), and the resistance of the scope termination, $R_{\text{scope}}=50$ Ω. The approximate form of Eq. (3) becomes

$$V \approx R_{\text{scope}} \frac{\cos(\theta_{\text{view}})}{R^2} \pi(S/2)^2 W_s H_d \left(\frac{R}{R+D}\right)$$
$$\times \int \bar{L}(\lambda,t)T_{\text{filter}}(\lambda)\epsilon_{\text{grating}}(\lambda)\rho_{\text{diode}}(\lambda,t)d\lambda, \tag{3}$$

where geometric factors, treated as wavelength independent, have been moved outside the integral. The transmission filter and grating should not influence the time response of the instrument to the incoming radiation.

For the filter transmission, grating efficiency, and diode responsivity in Eq. (3), a calibration effort was required. Each component of the spectrometer has been characterized at the X24C beamline of the National Synchrotron Light Source at Brookhaven National Laboratory. This beamline is equipped with a scanning monochromator capable of a spectral resolving power of $\sim$1000 over an energy range of 5 eV to 1 keV.[17] The Ti transmission filter, the Au transmission grating, and the Si photodiode array were each studied in similar manner. A NIST-calibrated reference photodiode [type AXUV-100G from International Radiation Detectors (IRD)] was used to measure the soft x-ray flux passed by the monochromator at a chosen energy and compared to similar results with the test component inserted into the light path. For the transmission filter and transmission grating, the mea-
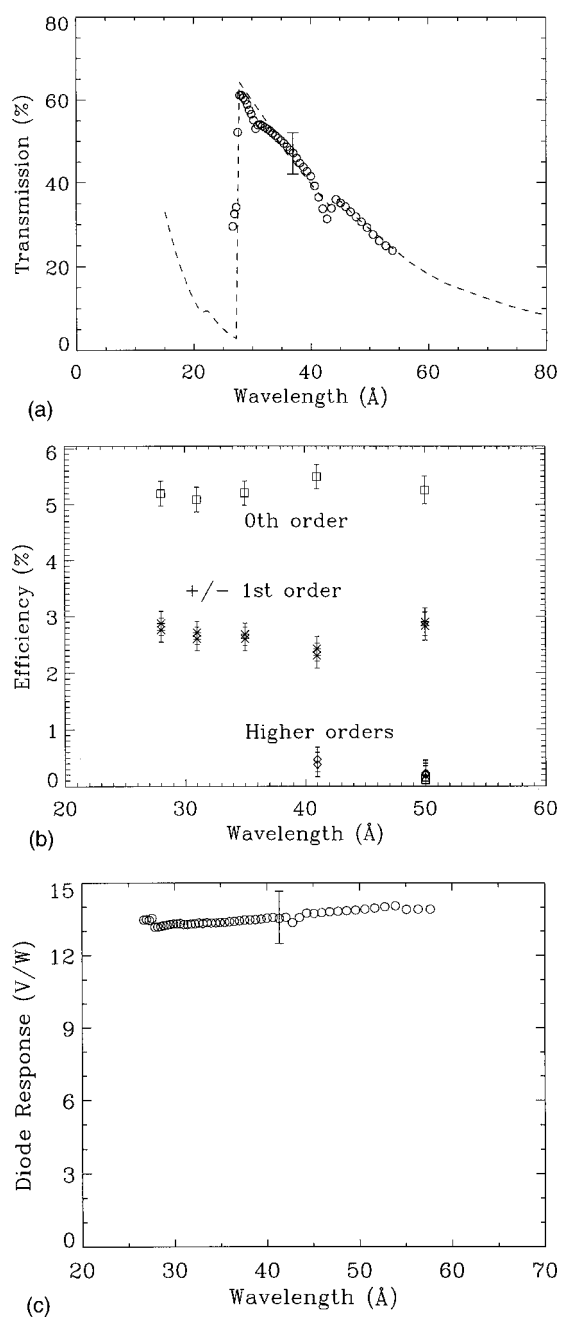
FIG. 2. The measurement of absolute intensity requires the calibration of the transmission filter, the transmission grating, and Si photodiode. Part (a) compares the measured transmission efficiency of the titanium filter to a theoretical curve that assumes a 2600 Å thick layer of Ti with a 50 Å layer of C (from contamination) on each surface. Part (b) compares the transmission efficiency of various orders of the diffraction grating to a model based on scalar diffraction theory. Part (c) presents the Si photodiode calibration.

surement used the same reference detector for both measurements. The calibration of the spectrometer's photodiode responsivity was determined relative to the known responsivity of the reference detector.

The calibration of the transmission filter and the transmission grating measured the percentage of light transmitted through the given component. The result for the Ti filter is shown in Fig. 2(a) with a calculation based on the data of Henke.[18] The Ti filter has strong wavelength dependence due to the L edge in Ti at 27.2 Å and has two small dips at 43.6

Å and 31.0 Å that are due to the residual presence of carbon and nitrogen contaminants. The best match between theory and experiment assumed a 2600 Å thick free-standing Ti foil with a thin 50 Å contamination layer of C on each surface. The filter transmits the desired radiation with wavelength above the Ti L edge at 27.2 Å and attenuates shorter wavelength radiation that would appear in higher diffraction orders at the same detector position as the desired radiation. From previous measurements of W and Au spectra, it was known that radiation in the short wavelength region can be significant and, if the transmission grating passes higher diffraction orders, the long wavelength data can be compromised by the shorter wavelength radiation.

Figure 2(b) presents the calibration of the transmission grating. This graph was produced by recording two measurements at each wavelength of interest. The first measurement was the reference diode current without the diffraction grating placed in the path of the monochromator beam. The second measurement was obtained by swinging the reference detector in an arc about the centerline of the transmission grating to observe the variation in diode current with diffraction angle. The ratio of these two measurements (corrected for changes in the synchrotron beam current) yielded the dependence of efficiency on transmission angle. The peaks in this curve were then fit with Gaussian functions. The peak values for the Gaussian yielded the values plotted in Fig. 2(b). The diffraction efficiency of the transmission grating was not found to depend on the region of the grating that was illuminated by the 1 mm^2 monochromator beam. An important result apparent in Fig. 2(b) is that the first order transmission efficiency dominates that of the higher diffraction orders. If all the diffraction orders are taken into account, then the total fraction of light transmitted by the grating is ~12% for the wavelengths shown. This value is largely determined by the fraction of the transmission grating surface unobscured by the gold bars of the transmission grating and the support meshes. These observations show that the transmission grating has approximately constant diffraction efficiency over the 4.7 Å wavelength range covered by a single diode.

The measurements for the Si photodiodes were done in much the manner as the previous two calibrations with some additional steps taken to further ensure reliable values. The abovementioned photodiode array (AXUV-100G) used in the experiments is currently not compatible with the strict vacuum requirements and scanning mechanisms in use at the X24C beamline. Consequently, measurements were made on a single 1 mm^2 diode with identical size and construction (an IRD model AXUV HS-5). This diode and the reference diode had identical 0.79 mm diameter pinholes so that the same area on each diode was illuminated. The relative response of the two diodes demonstrated that the two agree to within ~5%. Both the reference AXUV HS-5 diode and the spectrometer's AXUV-100G diode array have been extensively calibrated at other synchrotrons.[19,20] Based on these calibrations, the response expected for the photodiode array is shown in Fig. 2(c).

A final concern is the expected time response of the diodes. During the calibrations described above, the reference

diode is typically operated with no bias, and the diode current is recorded by a time-integrated electrometer. As a check of this procedure, the electrometer was replaced with a fast oscilloscope (1 GHz band pass) and a high gain amplifier ($G=794$). The diode was reverse biased to 45 V to improve its time response and the oscilloscope recorded the diode current pulse due to the individual electron bunches of the synchrotron beam.

The comparison to the usual time-integrated calibration (for the same photon energy incident on the diodes) is based on the fraction of time that the diode is exposed to the radiation. The synchrotron beam contains $N_{pulse}=25$ electron bunches periodically spaced at $T_{period}=19$ ns. The diode pulse from a single electron bunch had a duration of $T_{pulse}=2$ ns (FWHM of observed diode signal). The 25 electron bunches are followed by 5 "empty" bunches of total duration 95 ns. The entire pulse train ($N_{total}=30$ bunches) passes by the entrance of the X24C beamline every 570 ns. From these values for the pulse timing, the equivalent time-integrated current result can be estimated from the magnitude of the voltage pulse on the oscilloscope ($V_{scope}\sim24$ mV, $R_{scope}\sim50$ Ω):

$$I\approx(V_{scope}/G\cdot R_{scope})\cdot(N_{pulses}/N_{total})\cdot(T_{pulse}/T_{period})$$
$$\approx53\ \text{nA}. \quad (4)$$

The comparable electrometer result was 55 nA. This indicates that the current collected from the 1 mm^2 diode in pulsed mode is essentially equal to the current collected in the time-integrated mode.

The results of the calibration enable further simplification of the measurement equation from the form of Eq. (3). Since the band pass of each diode is small (~4.7 Å), the variation in the filter, grating, and diode elements with wavelength is not important except near an absorption edge in the transmission filter, e.g., near 27.2 Å for the Ti filter. Equation (4) can then be written as

$$V(t)\approx R_{scope}\frac{\cos(\theta_{view})}{R^2}\pi(S/2)^2W_sH_d\left(\frac{R}{R+D}\right)$$
$$\times T_{filter}(\lambda)\epsilon_{grating}(\lambda)\rho_{diode}(\lambda,t)\int\bar{L}(\lambda,t)d\lambda. \quad (5)$$

The measured diode voltage will be interpreted as the spectral radiance integrated over the field of view and over the wavelength band pass of the photodiode. Although the synchrotron measurements indicate that the time dependence of the diode response should not affect the results strongly, this assumption will be checked by comparing the relative time histories of the streak camera signal and the photodiode signal. For the experiments presented in this paper, a large reverse bias (90 V) was used to maximize the time response of the photodiodes.

IV. RESULTS

Because each diode sensed the soft x-ray flux for a 4.7 Å wide spectral interval, preliminary presentations of time integrated spectra will help serve to orient the discussion of the
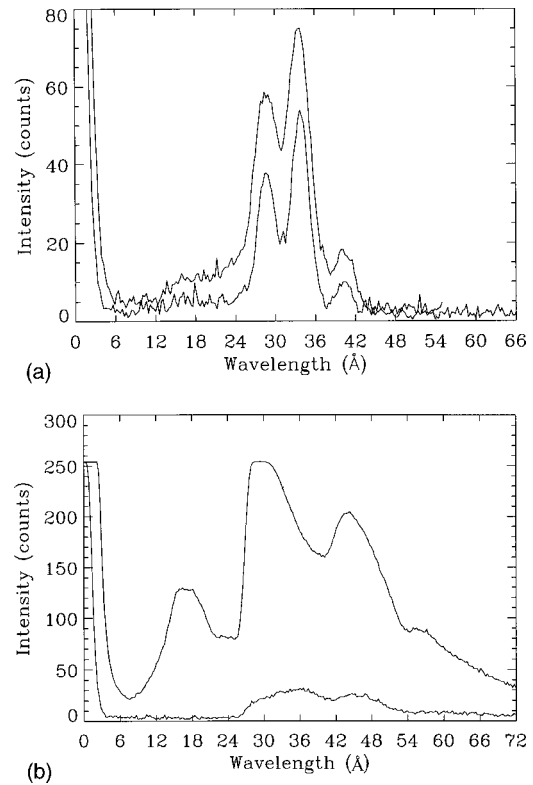

(a)

(b)

FIG. 3. Spectra from CH (a) are shown for two different laser power densities. The upper solid curve in each plot presents the time-integrated CCD spectrum for a ten beam shot and the lower solid curve presents the CCD spectrum for a three beam shot. The dashed line in each figure shows the time-integrated spectrum from the streak camera for the same three beam shot. The streak camera intensity has been renormalized for comparison to the CCD result. Spectra from Au targets (b) are shown for two different laser power densities with the same conventions as (a). The pronounced dip in intensity in the wavelength range from 24 to 27 Å is due to the L edge of the Ti filter.

diode results. In Fig. 3(a), time-integrated spectra from the CCD camera are shown for a CH target irradiated with a laser power density of 6×10^{12} W cm^{-2} and 15×10^{12} W cm^{-2}. Discrete lines are observed: the L_α and L_β lines of the hydrogenlike carbon and the $1s^2$-$1s2p$ resonance line of the heliumlike carbon. Due to the 27.2 Å cutoff of the Ti filter, lines and free-bound continuum at shorter wavelengths are not observed. It is also clear from these spectra that radiation from the second diffraction order of the grating is not significant. The apparently large signal in the free-bound continuum below the filter edge has been shown to be due to the combination of the low instrumental resolution and the increased transmission efficiency of the diffraction gratings.[21] Finally the linewidths (FWHM) are 3.1 Å for the CCD spectra, in good agreement with Eq. (1). Sample time-integrated Au spectra are shown in Fig. 3(b). These spectra do not show discrete lines but radiation from the N and O bands of Au. A sharp cutoff is seen due to the filter edge. Although the sensitivity of the CCD is not calibrated, as expected the high-Z targets radiate much more strongly than the low-Z targets.

Figure 4(a) shows the complete set of diode data for a Au target irradiated with a laser power density of 1.6 $\times10^{13}$ W cm^{-2} plotted in units of absolute flux versus time
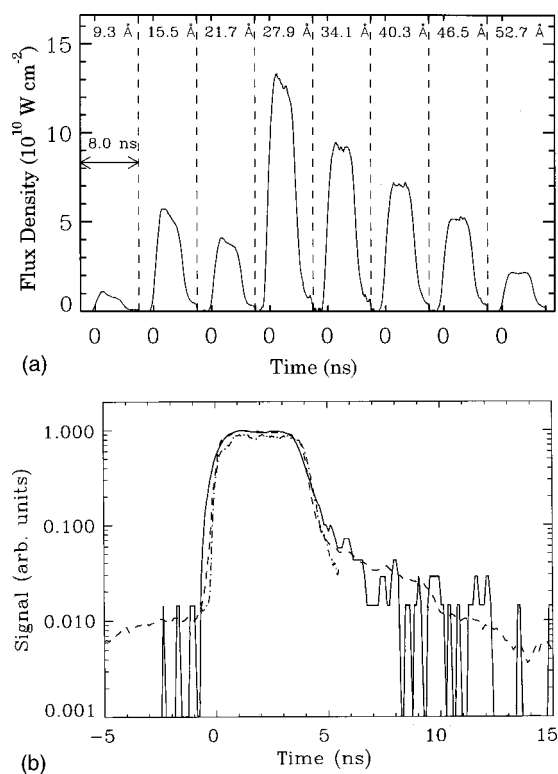
FIG. 4. (a) Shows the calibrated radiation flux as a function of time as measured by each element of the photodiode array for a high laser power (1.6×10^{13} W/cm^2) shot with an Au target. The graph shows time along the abscissa and signal along the ordinate. The central wavelength for each diode is indicated above the respective time history. The diode signals have not been corrected for the Ti filter transmission. (b) Compares the time response of the photodiode centered at 3.41 Å (solid line) to the laser pulse shape (dashed line) and the streak camera (dot-dashed line). The streak camera signal was binned over the wavelength range of the photodiode. All three signals were renormalized to facilitate comparison.

FIG. 5. Calibrated radiation flux as a function of time for a CH target at low laser power density (6.0×10^{12} W/cm^2) is presented with the same conventions as Fig. 4. The comparison of the diode signal, laser pulse, and streak camera response in (b) is for the fifth photodiode at 34.1 Å. The comparison of the photodiode and streak camera signals shows that radiation persists for a significant time after the main laser pulse.

but without the correction for the Ti transmission filter. In this plot, time is along the abscissa and diode signal is along the ordinate. The diodes have been ordered in increasing wavelength with the central wavelength of each diode shown above the corresponding time history. A vertical dashed line indicates the separation of the abscissa between the adjacent diode channels. The relative magnitude is clearly affected by the wavelength dependence of the Ti transmission filter. The intensity distribution for the diodes is consistent with the time-integrated spectrum from the CCD with the lower spectral resolution of the diodes is taken into account. For this shot, the diodes were positioned such that diodes 5 through 8 were located at wavelengths above the filter cutoff. The streak camera and diode data show similar time histories. Figure 4(b) compares the data taken from the diode centered at 34.1 Å of Au with the corresponding streak data (summed over the wavelength range of the diode), and the laser pulse shape. The streak camera data and the laser pulse shape were renormalized to match the peak of the diode data. The three signals show strong correlation. This result shows that the plasma formation and recombination occur rapidly with the application or cessation of laser energy. The time response of the photodiodes is adequate for the experiment.

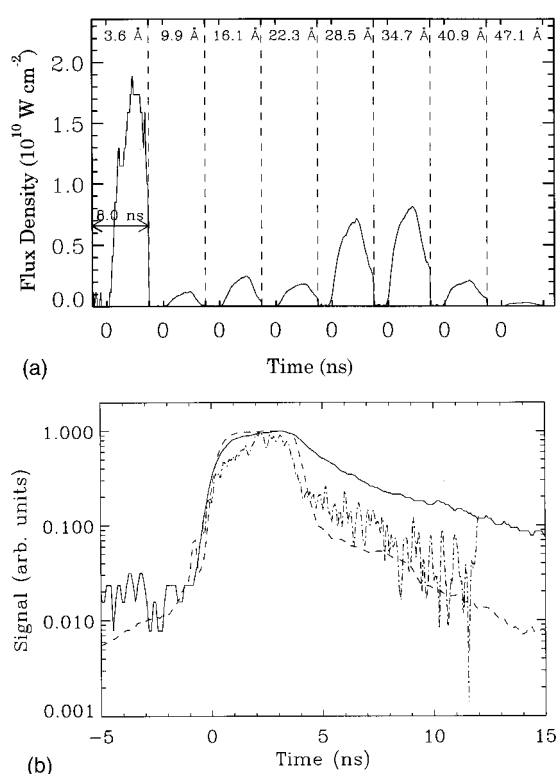Figure 5 presents a similar set of data for a CH target, at

a laser power density of 4.3×10^{12} W cm^{-2}. In Fig. 5(b), a comparison of the streak camera, Si photodiode, and laser pulse shape is made for diode centered at 32.2 Å. The streak camera and diode signal show a strong correlation for the duration of the laser pulse but show significant flux long after the end of the laser pulse. The relatively slow rate of recombination for CH targets after the end of the laser pulse has been a long known phenomenon.[22] It will be the topic of a separate paper since the current work focuses on data relevant to the laser-matter interactions pertinent to target compression for inertial confinement fusion.

V. DISCUSSION

Although this paper primarily focuses on the experimental results from the absolutely calibrated spectrometer, a brief description of the theoretical effort and preliminary comparison to simulation results are included in this section for completeness. A more elaborate model, and more detailed conclusions, will be described in another paper. The model describes emission from a supposed planar target irradiated by the experimental laser intensity according to a 1D version of the FAST code developed at NRL.[23,24] FAST provides a multidimensional treatment of hydrodynamics and radiation transport, primarily for the target physics relevant to inertial confinement fusion. Detailed discussions of the FAST code have been previously published with successful comparison to hydrodynamic experiments such as growth of the

Rayleigh–Taylor instability.[23] Since the present paper is concerned with the radiation, the discussion will be limited to that aspect of the code. The radiation transport package uses a multigroup diffusion model with a variable Eddington factor. The necessary opacities are based upon Busquet's non-local thermal equilibrium (NLTE) model (RADIOM)[25] which estimates the required values from results calculated for local thermodynamic equilibrium (LTE), but at an effective ionization temperature T_z. An algorithm to evaluate T_z, as a function of the electron temperature, density, and radiation field, for each plasma cell, at each time step has been introduced in FAST.[26] The LTE opacities are computed with the super transition array (STA) model,[27,28] which was successfully compared to experimental LTE opacities.[29] An auxiliary code (MIX) is used for generating tables of Rosseland and Planck opacities for arbitrary photon groups and mixtures of elements. These tables are loaded into FAST. The present simulations used 98 groups, several of them around carbon resonance lines.

Let us note that comparisons of theoretical with experimental absolute emission are rare, because the two sides are equally difficult to access. On the experimental side, in the present case, two issues need to be addressed. First, the angular and spatial distribution of radiation is problematic since the one-dimensional simulations do not provide such multidimensional information. The simulations yield a value for the exitance from the target plasma along the target normal $[M_{sim}(\lambda)$ in W cm^{-2} Å$^{-1}]$ while the measurement equation developed in Sec. III needs the target radiation (W cm^{-2} Å^{-1} ster^{-1}) averaged for the diagnostic's field of view, a view that is well separated from the target normal. The target radiation has been assumed to be emitted isotropically from a uniform disk with diameter equal to that of the laser focal spot. The average radiance in Eq. (5), $\bar{L}$, will then be given by $M_{sim}(\lambda)/\pi$. Second, two effects of the modest spectral resolution for the instrument need to be taken into account. The theoretical spectrum must be convolved with a Gaussian function with a 3.03 Å FWHM to account for the finite width of the entrance slit (see Secs. II and IV). The finite width of the diodes must also be accounted for by calculating the integral of the simulated intensity over the wavelength range of each diode as was indicated in Eq. (5).

On the theory side, the approximations are numerous: the target is assumed to remain 1D planar throughout the laser pulse, the edge effects being neglected, the radiation transport is based on the diffusion approximation, and, importantly, Busquet's model is only approximate. The model is less reliable for emissivity than for absorption[30] because the non-LTE effects are subsumed in one parameter, the ionization temperature T_z. The individual emitting atomic levels are supposed to follow a Boltzmann population distribution at T_z. For instance, the incident radiation field changes only the overall charge distribution, but does not influence the population of the emitting levels. This is because the present simulations do not involve post-processing, where the atomic physics is solved taking into account the temperature, density, and radiation field and does not follow the time history and spatial dependence. The latter point is deliberate,
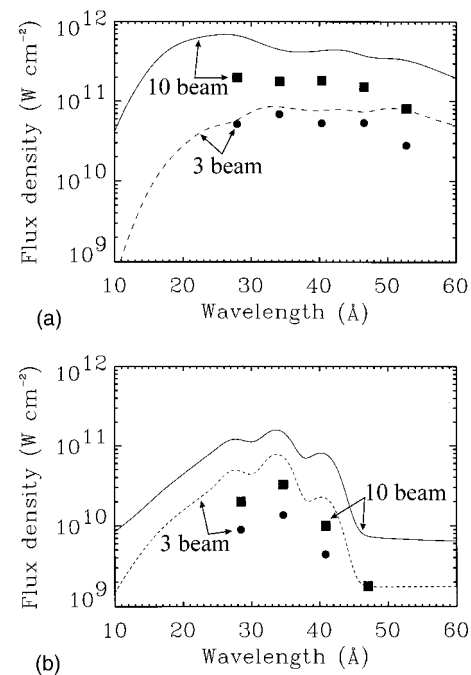

FIG. 6. Comparisons of time-integrated results from theory and experiment are shown for Au (a) and CH (b). The solid lines represent the theoretical spectral energy density for high laser power density (Au: 1.6 $\times 10^{13}$ W cm^{-2}; CH: 1.7×10^{13} W cm^{-2}) and the dashed lines represent the theoretical spectra at low laser power density (Au: 6.4×10^{12} W cm^{-2}; CH: 6.0×10^{12} W cm^{-2}). The symbols on the plots represent the time-integrated energy flux density measured by several of the Si photodiodes. The filled squares are to be compared to the higher laser power density (i.e., the solid lines) and the filled circles are to be compared to the lower laser power density (i.e., the dashed lines). The theoretical curves have been convolved with a 3 Å wide (FWHM) Gaussian instrumental function to facilitate comparison.

since the aim of the present comparison is to test the radiation package in the FAST code. With these caveats in mind, we can compare time integrated experimental data with the simulations.

Figure 6(a) compares the diode data with time integrated spectra produced by the codes for a Au target irradiated with a laser power density of 5.4×10^{12} W cm^{-2} (three beams) and 2.0×10^{13} W cm^{-2} (ten beams). These simulated spectra are shown as dashed and solid lines, respectively. Since each diode signal represents the total flux over a 4.7 Å region, the measured values (filled circles and squares) are shown as discrete points in Fig. 6. The circles correspond a lower laser irradiance $(6.4 \times 10^{12}$ W cm$^{-2})$ while the squares correspond to the higher irradiance $(1.6 \times 10^{13}$ W cm$^{-2})$. Both the simulated and measured values represent the flux density averaged from 1.5 to 2.0 ns during the laser pulse. The experimental results for the Au targets are in good overall agreement with the theoretical values in that the ratio is between 1.1 and 2.8 for the three beam case and between 2.3 and 4.1 for the ten beam case. Diodes at wavelengths below the filter edge are not shown since the filter calibration did not extend below 25 Å. The diode centered at 27.9 Å has larger error than the other diodes due to the L edge of the Ti filter. If the dominant errors are due to the geometric factors and the component calibrations, then the measurements are accurate to approximately 25%.

A similar comparison is shown in Fig. 6(b) for CH targets irradiated with laser power densities 6.0×10^{-12} W cm^{-2} (circles) and 1.7×10^{13} W cm^{-2} (squares) for consistency with the Au experiments. The laser irradiances for the simulations are 6.1×10^{12} W cm^{-2} (dashed line) and 2.0×10^{13} W cm^{-2} (solid line). The data were again averaged over the period from 1.5 to 2.0 ns. This time range excludes the weaker late-time emission as illustrated in Fig. 5(b), that is not treated by the 1D modeling of the laser-plasma interaction. The ratio of theory to experiment shows the theory is again (away from the filter edge) higher by a factor ~5.3 for the three beam case and between 4.5 and 7.8 for the ten beam case.

It can be noted that the simulations are always higher than the experiments. This can be attributed to several causes. One is the fact that 1D modeling assumes a constant temperature on the radiating surface. In reality, the plasma surface does not remain planar, and the temperature is lower at the edges than in the center. Indeed, the laser spot is 750 μm in diameter, but the target size is $\approx$3 mm. This so called "edge effect" diminishes the total radiation. Another reason is that Busquet's model tends to overestimate the temperature.[26] We also note that the discrepancy is larger for CH than for Au. This we tentatively attribute to the following reason: the Au spectra are quasi-continua emitted by atomic systems with an extremely large number of energy-near atomic levels. In this case, the approximation of a pseudo-Boltzmann distribution is warranted. On the other hand, for H-like or He-like carbon, there are only a few resonant levels, and the model of Busquet is probably less applicable. We do not know at this point what is the effect of the modified diffusion approximation on the total emitted radiation, and if it affects differently CH and Au. Obviously, more elaborate models are needed to pinpoint the sources of the discrepancy.

Future experiments will be performed to determine the spatial and angular distribution of the radiation but the agreement is considered to be reasonable considering the 1D modeling used for the numerical result and the assumptions involved with the treatment of the diode data discussed in the previous section. The positive outcome of these experiments is the incentive for developing better models for radiation emission and transport. Indeed we plan to implement a collisional radiative model (SCROLL)[30] in the near future in order to redo these simulations.

VI. SUMMARY

Soft x-rays in the range of 10 to 60 Å have been measured at the Nike laser facility using a transmission grating spectrometer. Key components of this spectrometer have been calibrated at the X24C beamline of the NSLS at Brookhaven National Laboratory. The spectrometer has recorded spatially integrated, time resolved spectra from CH and Au targets and for two laser power densities. The main purpose of these experiments was to provide experimental verification of numerical codes used to predict the performance of inertial fusion targets. The time integrated fluxes from Au targets are in good overall agreement with the theoretical predictions (theory/experiment ~1–4). The time re-

solved data from the diodes showed that the soft x-ray radiation was well correlated to the laser pulse. The time-integrated results from the CH targets showed a discrepancy between the experiment and theory. The predicted values were higher than the experimental values by a factor between 5 and 8. The time resolved data from the CH targets also indicate emissions after the laser pulse that has not been incorporated into the theoretical predictions. This discrepancy may be explained in part by edge effects, and in part by the inaccuracy of the non-LTE model. We plan to implement a better model[31,32] in the near future.

[1]D. R. Kania, H. Kornblum, B. A. Hammel, J. Seely, C. Brown, U. Feldman, G. Glendinning, P. Young, E. Hsieh, M. Hennesian, L. DaSilva, B. J. McGowan, D. S. Montgomery, C. A. Back, R. Doyas, J. Edwards, and R. W. Lee, Phys. Rev. A **46**, 7853 (1992).

[2]T. Mochizuki, T. Yabe, K. Okada, M. Hamda, N. Ikeda, S. Kiyokawa, and C. Yamanaka, Phys. Rev. A **33**, 525 (1986).

[3]S. E. Bodner, D. G. Colombant, J. H. Gardner, R. H. Lehmberg, S. P. Obenschain, L. Phillips, A. J. Schmitt, J. D. Sethian, R. L. McCrory, W. Seka, C. P. Verdon, J. P. Knauer, B. B. Afeyan, and H. T. Powell, Phys. Plasmas **5**, 1901 (1998).

[4]D. G. Colombant, S. E. Bodner, A. J. Schmitt, M. Klapisch, J. H. Gardner, Y. Aglitskiy, A. V. Deniz, S. P. Obenschain, C. J. Pawley, V. Serlin, and J. L. Weaver, Phys. Plasmas **7**, 2046 (2000).

[5]H. Gursky and H. Zehnpfennig, Appl. Opt. **5**, 875 (1966).

[6]N. M. Ceglio, R. L. Kauffman, A. M. Hawryluk, and H. Medecki, Appl. Opt. **22**, 318 (1983).

[7]M. Chaker, V. Bareau, J. C. Kieffer, H. Pepin, and T. W. Johnston, Rev. Sci. Instrum. **60**, 3386 (1989).

[8]K. F. Fischbach, A. M. Levine, M. L. Schattenburg, D. Dewey, R. L. Renshaw, J. Dalcanton, R. Newman, and W. Fissel, SPIE: X-ray Instrumentation in Astronomy II **982**, 273 (1988).

[9]T. Wilhein, S. Rehbein, D. Hambach, M. Berglund, L. Rymell, and H. M. Hertz, Rev. Sci. Instrum. **70**, 1694 (1999).

[10]S. A. Bel'kov, B. A. Bryunetkin, N. V. Zhidkov, I. Yu. Skobelev, N. A. Suslov, and A. Ya Faenov, Quantum Electron. **24**, 234 (1994).

[11]J. L. Bourgade, P. Combis, M. Louis-Jacquet, J. P. Le Breton, J. de Mascureau, D. Naccache, R. Sauneuf, G. Thiell, C. Keane, B. MacGowan, and D. Matthews, Rev. Sci. Instrum. **59**, 1840 (1988).

[12]K. Eidmann, T. Kishimoto, P. Herrmann, J. Mizui, R. Pakula, R. Sigel, and S. Witkowski, Laser Part. Beams **4**, 521 (1986).

[13]J. F. Pelletier, M. Chaker, and J. C. Kieffer, J. X-Ray Sci. Technol. **6**, 359 (1996).

[14]P. Predehl, H. Bräuninger, W. Burkart, B. Aschenbach, J. Trümper, M. Kühne, and P. Müller, SPIE: X-ray Instrumentation in Astronomy II **982**, 265 (1988).

[15]F. Grum and E. J. Becherer, *Optical Radiation Measurements, Vol. 1. Radiometry* (Academic, New York, 1979).

[16]C. Brown, J. Seely, U. Feldman, S. Obenschain, S. Bodner, C. Pawley, K. Gerber, V. Serlin, J. Sethian, Y. Aglitskiy, T. Lehecka, and G. Holland, Rev. Sci. Instrum. **68**, 1099 (1997).

[17]W. R. Hunter, R. T. Williams, J. C. Rife, J. P. Kirkland, and M. N. Kabler, Nucl. Instrum. Methods **195**, 141 (1982).

[18]B. L. Henke, E. M. Gullikson, and J. C. Davis, At. Data Nucl. Data Tables **54**, 181 (1993).

[19] L. R. Canfield, J. Kerner, and R. Korde, Appl. Opt. **28**, 3940 (1989).

[20] F. Scholze, H. Rabus, and G. Ulm, Appl. Phys. Lett. **69**, 2974 (1996).

[21] J. L. Weaver, G. Holland, U. Feldman, J. F. Seely, C. M. Brown, V. Serlin, A. V. Deniz, and M. Klapisch, Rev. Sci. Instrum. **72**, 108 (2001).

[22] B. C. Boland, F. E. Irons, and R. W. P. McWhirter, J. Phys. B **2**, 1180 (1968).

[23] J. H. Gardner, A. J. Schmitt, J. P. Dahlburg, C. J. Pawley, S. E. Bodner, S. P. Obenschain, V. Serlin, and Y. Aglitskiy, Phys. Plasmas **5**, 1935 (1998).

[24] J. P. Boris and D. L. Book, J. Comput. Phys. **11**, 38 (1973).

[25] M. Busquet, Phys. Fluids B **5**, 4191 (1993).

[26] M. Klapisch, A. Bar-Shalom, J. Oreg, and D. Colombant, Phys. Plasmas **5**, 1919 (1998).

[27] A. Bar-Shalom, J. Oreg, W. H. Goldstein, D. Shvarts, and A. Zigler, Phys. Rev. A **40**, 3183 (1989).

[28] D. Colombant, M. Klapisch, and A. Bar-Shalom, Phys. Rev. E **57**, 3411 (1998).

[29] P. T. Springer, D. J. Fields, B. G. Wilson, J. K. Nash, W. H. Goldstein, C. A. Iglesias, F. J. Rogers, J. K. Swenson, M. H. Chen, A. Bar-Shalom, and R. E. Stewart, Phys. Rev. Lett. **69**, 3735 (1992).

[30] M. Klapisch and A. Bar-Shalom, J. Quant. Spectrosc. Radiat. Transf. **58**, 687 (1997).

[31] A. Bar-Shalom, J. Oreg, and M. Klapisch, Phys. Rev. E **56**, R70 (1997).

[32] A. Bar-Shalom, J. Oreg, and M. Klapisch, J. Quant. Spectrosc. Radiat. Transf. **58**, 427 (1997).